

Contents lists available at ScienceDirect

Acta Materialia

journal homepage: www.elsevier.com/locate/actamat



Stability of oxide-sulfate mixtures and implications for deposit-induced degradation of advanced alloys and coatings



Atharva S. Chikhalikar¹, Eeshani P. Godbole¹, David L. Poerschke*

Department of Chemical Engineering and Materials Science, University of Minnesota, Minneapolis, MN, USA

ARTICLE INFO

Article history:
Received 19 April 2022
Revised 11 July 2022
Accepted 16 July 2022
Available online 17 July 2022

Keywords: Corrosion Thermodynamic Modeling Phase stability Decomposition Sulfates

ABSTRACT

Turbine engines ingest atmospheric aerosols that include multi-cation oxide-sulfate mixtures, which deposit onto surfaces within the engine. These deposits are often implicated in hot corrosion of alloys and bond coats and can accelerate thermomechanical failure of ceramic coatings through reaction and infiltration mechanisms. Understanding the intrinsic stability of oxide-sulfate deposits, including the tendency for sulfate decomposition, is important to identify efficient testing protocols. This work addresses that need by integrating experiments and computational thermodynamics models to systematically analyze the effect of deposit composition and temperature on the sulfate decomposition and melting behavior of five model mixed-anion deposits. Mass loss analysis and energy dispersive x-ray spectroscopy show that sulfate decomposition occurs much faster in the mixtures compared to pure calcium sulfate. The thermodynamic computations show that reaction pathways forming ternary and quaternary silicates accelerate sulfate decomposition faster than those forming binary reaction products. The results also show that multi-cation mixtures can suppress the evaporation of sodium and potassium sulfates, retaining the sulfate-bearing liquid to higher temperatures. The results can be used to differentiate the behavior of sulfate-, sulfate-oxide-, and oxide-based deposits, and to guide the discovery of new high temperature alloys and coating materials.

© 2022 Acta Materialia Inc. Published by Elsevier Ltd. All rights reserved.

1. Introduction

Materials in turbine engines must withstand cyclic high temperatures and mechanical stresses while resisting oxidation and corrosion in the combustion environment. The accumulation of corrosive deposits formed from ingested aerosols (salts, dusts, ashes, etc.) causes premature failure by accelerating oxidation and amplifying thermo-cyclic stresses. Mitigating this degradation is a core challenge driving the development of advanced coating materials and architectures to protect alloys and ceramic composites.

Historically, deposit-induced degradation has been divided into two categories. The first is hot corrosion (HC) of alloys by Na_2SO_4 -based deposits, which predominates in the range 600 °C to 950 °C. Around 850 °C, Na_2SO_4 melts and fluxes the protective thermally grown oxide (TGO), accelerating oxidation and sulfidation of the alloy (Type-I HC) [1]. At lower temperatures (around 700 °C), high SO_3 partial pressure (p_{SO_3}) can stabilize eutectic melts between Na_2SO_4 and (SO_4), leading to severe alloy pitting (Type-II HC) [2–4]. Above 950 °C pure Na_2SO_4 doesn't condense (or evaporates),

E-mail addresses: dpoersch@umn.edu, poerschke@umn.edu (D.L. Poerschke).

diminishing its role in alloy oxidation and corrosion. Thus, the intrinsic oxidation kinetics of the alloy, rather than deposit-induced corrosion, are often thought to dominate at higher temperatures. Hot corrosion research has traditionally focused on understanding the influence of alloy composition and atmosphere chemistry, with less emphasis on variations in the deposit composition.

The second category comprises degradation induced by oxide-based calcium-magnesium-iron-aluminosilicate (CMFAS²) deposits [5–10]. Because the CMFAS deposits don't typically melt below 1150 °C, they are a more significant threat to ceramic thermal and environmental barrier coatings (TBC, EBC) operating at higher temperatures than to the underlying alloys or composites. The CMFAS melts infiltrate porous TBCs, leading to loss of coating compliance and higher thermal stresses on cooling [11]. They also react with EBC materials to produce reaction products with less desirable thermal properties [12–15]. The research community studying CMFAS degradation has identified important effects related to changes in the CaO:SiO₂ ratio and the presence of secondary com-

^{*} Corresponding author.

¹ Authors contributed equally.

 $^{^2}$ Deposit compositions are abbreviated using modified cement chemistry notation wherein the first letter of the cation symbol is used to denote oxides using single cation formulae (C = CaO, A = AlO $_{15}$, S = SiO $_{2}$, etc.) and \bar{S} denotes the sulfate anion. CMFAS, rather than CMAS, captures Fe as an important cation constituent.

ponents (e.g., MgO, Fe $_2$ O $_3$, Al $_2$ O $_3$, Na $_2$ O, K $_2$ O, etc.) on deposit melting and reactivity [5,7,16–21]. Some reports show that these oxide deposits can also accelerate alloy oxidation by reacting with the Al $_2$ O $_3$ TGO to form less-protective oxides [22,23]. However, much of this research has focused on deposits comprised entirely of oxides.

There is growing evidence that multi-cation sulfate and mixed sulfate-oxide deposits, hereafter termed 'complex' deposits, threaten material durability via new mechanisms across a wide range of temperatures [24-29]. Many reports involve deposits containing CaSO₄, which may be ingested as gypsum or could form within the engine. Importantly, CaSO₄ accelerates alloy oxidation at temperatures above the typical Na₂SO₄ hot corrosion regime via reactions that convert the $\alpha\text{-Al}_2\text{O}_3$ TGO into a mixture of nonprotective calcium aluminates [29-32]. Accelerated alloy corrosion has also been observed in ex-service hardware in the vicinity of deposits containing a combination of cations including Ca, Al, Mg, and Si [32-34]. Similar effects have been confirmed in laboratory investigations of alloy oxidation in contact with mixed-oxide and oxide-sulfate-chloride deposits [24-26]. CaSO₄ has also been implicated in the infiltration and stiffening of TBCs operating at higher temperature [35,36].

Despite the apparent importance of complex deposits in materials performance, there are many unanswered questions about how and when reactions within mixed-anion deposits act either to accelerate or retard material degradation. For instance, if Na₂SO₄ promotes melting of CMFAS-type oxide deposits, TBC infiltration could occur at lower temperatures. The same mixed oxide-sulfate melt could also suppress Na₂SO₄ evaporation, extending alloy hot corrosion to higher temperatures. Likewise, CaSO₄ and MgSO₄ are more likely than Na₂SO₄ to decompose into the corresponding oxide and gaseous SO₂ and SO₃ (collectively SO_x) [37–43]. Decomposition of the sulfate has the benefit of removing sulfur from the deposit, potentially decreasing the tendency for alloy sulfidation, but the transient elevation in p_{SOx} near the alloy surface could activate other degradation pathways.

Developing the ability to differentiate when the sulfates in a complex deposit will decompose into their constituent oxides from scenarios in which the sulfates will be retained in the deposit is important to understand this degradation mechanism and to develop materials solutions. Within a turbine, the rate of sulfate decomposition is controlled by the equilibrium p_{SOx} above the decomposing sulfate and the rate at which saturated gas is diluted or swept away. Increasing the temperature accelerates sulfate decomposition by increasing the equilibrium p_{SOx} . Reactions between CaSO₄ and the TGO or oxide deposit components can also accelerate sulfate decomposition by producing reaction products with lower free energy than CaO. Prior work has shown that mixtures of CaSO₄ with SiO₂, Al₂O₃, or Fe₂O₃ exhibit higher p_{SOx} than pure CaSO₄ [40], likely driving faster decomposition. However, the specific reaction pathways and multi-cation oxides have not been systematically elucidated. The current work addresses that need by integrating experiments and computational thermodynamics models to understand how temperature and deposit constitution influence the sulfate stability.

2. Methods

2.1. Selection of representative mixed oxide-sulfate deposits

Eleven representative deposit compositions were selected to provide direct and systematic comparisons about the role of cation constitution and anion makeup (oxide and sulfate) on the deposit characteristics and reactivity. The three main parameters considered while defining cation ratios for the mixed deposits were: (i) Ca:Si ratio, which is known to influence apatite formation dur-

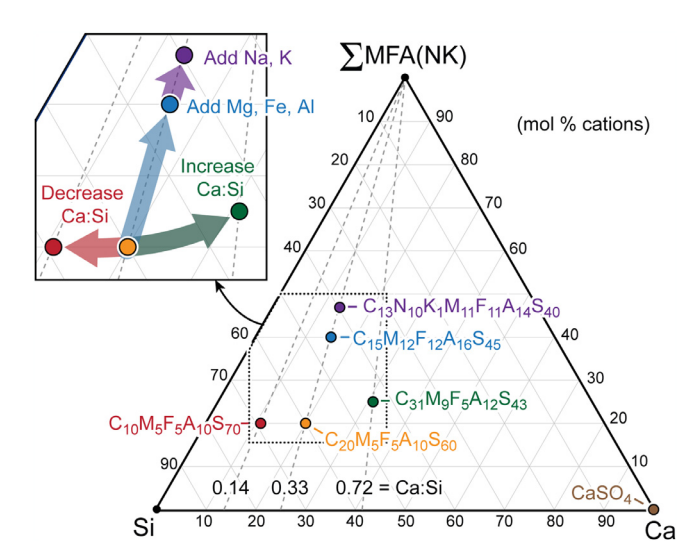


Fig. 1. Model deposit compositions were chosen to vary the cation contents to monitor the effect of the Ca:Si ratio, Mg, Al, Fe ion content and Na, K ion content.

ing CMAS reaction [5,17,18,20,44,45], (ii) total combined Mg²⁺, Fe^{2+/3+} and Al³⁺ content (\sum MFA), which are known to influence the melt properties and diversity in the crystalline reaction products [5,18,19], and (iii) the Na⁺ and K⁺ content (\sum NK) which are important in marine environments. Based on these parameters and knowledge from the CMFAS oxide literature, five master cation ratios were defined (Table 1, Fig. 1). The composition C₃₁M₉F₅A₁₂S₄₃ is based on observations of field hardware by Borom et al. [46] and has served as the basis for many synthetic laboratory deposits. C₁₀M₅F₅A₁₀S₇₀ and C₂₀M₅F₅A₁₀S₆₀ were originally defined by Summers et al. [47] to explore the effect of reducing the Ca:Si ratio relative to C₃₁M₉F₅A₁₂S₄₃. While keeping the Ca:Si ratio fixed, C₁₅M₁₂F₁₂A₁₆S₄₅ doubles the \sum MFA relative to C₂₀M₅F₅A₁₀S₆₀, and C₁₃N₁₀K₁M₁₁F₁₁A₁₄S₄₀ adds Na⁺ and K⁺ (\sum NK) approximating the Na:K ratio in seawater [48,49].

Two sets of deposits were synthesized using these 5 cation ratios. One set comprises just oxides (denoted -0) and the other set contains mixed oxides and sulfates (denoted -0 \bar{S}). For the mixed 0 \bar{S} deposits, Ca²⁺, Mg²⁺, Na⁺, and K⁺ were added in a 1:2 sulfate-to-oxide ratio and the Fe^{2+/3+}, Al³⁺, and Si⁴⁺ were added only as oxides. This constitution was based on the relative instability of iron, aluminum, and silicon sulfates relative to their oxides [38,50,51]. Thus, the latter cations are more likely to be present as oxides than sulfates in a turbine deposit. Indeed, studies of ex-service shipboard and aircraft engines have identified oxides and sulfates of Ca²⁺, Mg²⁺, Na⁺, and K⁺ in the deposits whereas Fe^{2+/3+}, Al³⁺, and Si⁴⁺ were present only as oxides [33,35,36]. Anhydrous CaSO₄ was used as a control.

2.2. Deposit synthesis and stability experiments

Given a wide range in melting and decomposition temperatures for the various constituents, a multi-step approach was developed to synthesize the mixed deposits (Fig. 2). The oxide mixtures were pre-reacted just below their incipient melting points, which are above the sulfate decomposition or melting temperatures. First, calcia (99.95% pure, Alfa Aesar (AA), Ward Hill, MA)), magnesia (98%, Acros Organics (AO), Morris Hill, NJ), alumina (99.95%, AA), and silica (99%, AA) were dried, calcined at 1100 °C, weighed in their required proportions, and mixed with iron(III) oxide (99.9%, AA). This oxide mixture was ball milled using alumina jars and milling media with ethanol as a dispersing medium. The CMFAS oxide mixtures were then pre-reacted for 24 h at either 1000 °C

Table 1 Summary of mixed deposit compositions.

Deposit Name	Ca:Si Ratio	$\sum MFA$ or $\sum MFANK$ (mol%)	Sulfates in <i>OS</i>	T _{solidus} for -0	T _{solidus} for - O \$
C ₁₀ M ₅ F ₅ A ₁₀ S ₇₀ *	0.14	20	CaSO ₄ , MgSO ₄	1186 °C	1186 °C
$C_{20}M_5F_5A_{10}S_{60}$	0.33	20	CaSO ₄ , MgSO ₄	1136 °C	1177 °C
$C_{31}M_9F_5A_{12}S_{43}$	0.72	26	CaSO ₄ , MgSO ₄	1220 °C	1136 °C
C ₁₅ M ₁₂ F ₁₂ A ₁₆ S ₄₅	0.33	40	CaSO ₄ , MgSO ₄	1186 °C	1186 °C
$C_{13}N_{10}K_1M_{11}F_{11}A_{14}S_{40}$	0.33	46	CaSO ₄ , MgSO ₄ , Na ₂ SO ₄ , K ₂ SO ₄	1065 °C	1065 °C
CaSO ₄	-	0	CaSO ₄	_	_

^{*} Corresponds to cation stoichiometry (mol%) 10Ca:5Mg:5Fe:10Al:70Si.

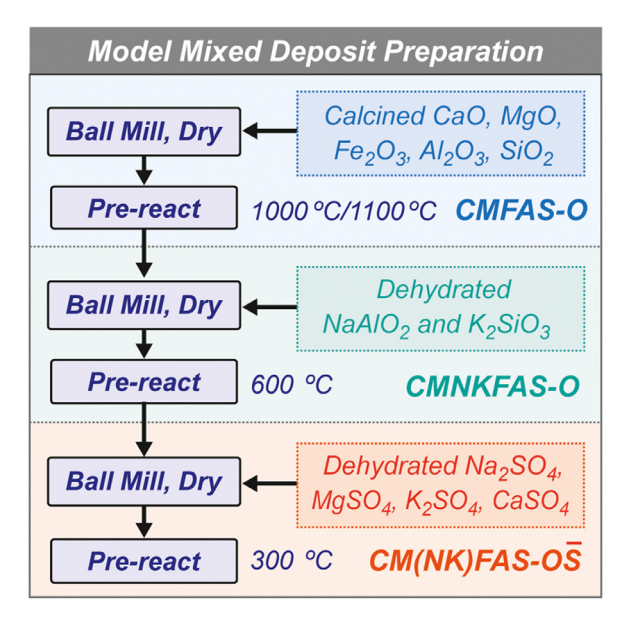


Fig. 2. Synthesis approach for the mixed anion deposits.

and 1100 °C, depending on the incipient melting temperature identified in preliminary experiments. Sodium aluminate (tech. grade, AA) and potassium silicate (2.5:1 wt.% $SiO_2:K_2O$, AA) were used as sources for sodium oxide and potassium oxide, given the reactive and corrosive nature of pure sodium and potassium oxides. These were dehydrated at 250 °C, added to the pre-reacted CMFAS oxide mixture, ball milled, and dried, followed by pre-reaction at 600 °C. For the oxide-sulfate mixtures, calcium, magnesium, sodium and potassium sulfates (CaSO₄ (99%, AO) MgSO₄ (99.5%, AA), Na₂SO₄ (99%, AO), and K_2SO_4 (99+%, AO)), were dehydrated at 300 °C, mixed with the pre-reacted oxides, ball milled, dried, and then pre-reacted at 300 °C.

To understand the intrinsic sulfate decomposition and melting behavior of the mixed $O\bar{S}$ deposits and CaSO₄, samples were subjected to 10 h isothermal heat treatments in dry air (< 6 ppm H₂O) at 50 °C increments between 725 °C and 1225 °C. (The actual temperatures are expected to be within $\pm 1\%$ of these setpoints for the calibrated tube furnaces). The pure oxide deposits were annealed for 10 h at 1225 °C as a baseline. A separate sample was used at each temperature, so the results represent the behavior at that temperature rather than cumulative behavior. Cold-pressed 6 mm diameter pellets weighing approximately 100 mg were placed in individual platinum foil cups within an alumina boat in a silica furnace tube. The samples were heated to the test temperature at 10 °C /min, held for 10 h, and cooled at a maximum rate of 8 °C /min in dry air flowing at 0.2 L/min. Separate furnace tubes and alumina boats were used for the O and $O\overline{S}$ samples, and those with or without Na and K to prevent cross-contamination. The pellet masses were recorded before and after each heat treatment using a balance with an accuracy of \pm 0.2 mg. Dehydration heat treatments at 300 °C were used to account for post-synthesis hydration of the sulfates during storage or handling. In several cases, multiple pellets of the same composition were tested in separate runs to ensure repeatability; the average of these runs is reported. The asprepared mixtures and the samples tested at 1125 °C were characterized using energy dispersive X-ray spectroscopy (EDS: Thermo-Noran Vantage system). The EDS analysis was performed on powdered samples and data was collected from several area scans to confirm the analysis was capturing the average characteristics of each sample. However, given challenges analyzing light elements the data was analyzed by comparing the normalized intensity of specific characteristic energies rather than by attempting full composition quantification.

2.3. Thermodynamic calculations

Computational thermodynamics models were used to interpret the experimental results and to provide deeper insights into the coupled roles of temperature and deposit composition on the decomposition of sulfates in mixed oxide-sulfate deposits. To match the experiments, calculations for mixed oxide-sulfate compositions used a 1:2 sulfate-to-oxide ratio for Ca²⁺, Mg²⁺, Na⁺, and K⁺, and Fe³⁺, Al³⁺, and Si⁴⁺ were added only oxides. Additional calculations described below used other combinations of oxides and sulfates to understand specific reaction pathways. The calculations employed the FactSage software package (FactSage Software, Thermfact/CRCT, Montreal, Canada) with the FTOxid and FactPS databases [52,53]. This combination of databases includes the relevant phases and gaseous species to predict the behavior of the mixed oxide-sulfate deposits. It was also used to calculate the deposit melting temperatures listed in Table 1.

Building on a previously described approach [54], the calculations were performed at 1 atm total pressure with the oxygen activity (p_{O2}) fixed at 0.21. After the temperature and the components of the oxide and sulfate mixture were defined,³ the equilibrium phases, phase fractions, component activities, and gas phase constitution were calculated and recorded for subsequent analysis. To determine the initial equilibrium p_{SOx} above each mixture (i.e., the p_{SOx} prior to sulfate decomposition), only enough air was added to stabilize the gas phase in equilibrium with the mixture.⁴

Then, to capture the transient nature of the sulfate decomposition, which is influenced by the equilibrium p_{SOx} and the rate at which SO_x is diluted or swept away, the calculations were repeated for progressively larger air-to-deposit ratios. To present the results,

³ Within the FactSage setup interface, 0.1 g of the condensed components were defined in the desired molar proportions. The results are presented on a normalized molar basis, thus the actual amount doesn't change the final calculation outcome.

 $^{^4}$ Recognizing that the p_{SO2} and p_{SO3} are defined by $SO_2+\frac{1}{2}$ $O_2\leftrightharpoons SO_3$ and $p_{SO2};p_{SO3}$ is fixed at a given temperature at constant p_{O2} , the results focus on $p_{SO2},$ which predominates for the conditions studied. For all calculations air was defined by adding N_2 with sufficient oxygen to maintain $p_{O2}=0.21.$

this reaction variable (i.e., the moles of air saturated with SO_{X} at the equilibrium $\mathrm{p}_{\mathrm{SOx}}$) is normalized based on the number of moles of sulfur in the system. This parameter, denoted $\chi_{\mathrm{air/S}}$ with units abbreviated mol./mol., is a geometry-independent proxy for the reaction time in a flowing system given that the sulfate decomposition rate (or time) is proportional to the product of the time-integrated instantaneous saturation concentration and the molar flow rate. In other words, the time required for sulfate decomposition scales with $\chi_{\mathrm{air/S}}$ if the molar flow rate is kept constant. The individual calculations within FactSage and the subsequent analysis were repeated to explore the effects of temperature, composition, and gas volume. This stepwise calculation approach reveals how the consumption of one or more of the reactants changes the decomposition driving force and the reaction pathway as sulfate decomposition proceeds.

Using these methods, three sets of calculations were performed:

- Initial p_{SOx} and reaction dynamics calculations for the five representative mixed-anion deposit compositions, which provide direct comparison with the experimental results.
- Reactions between CaSO₄ and individual oxide components in proportions corresponding to common reaction products identified in (1). These calculations reveal how specific reaction pathways influence the driving force for decomposition.
- 3. Systematic studies of the effect of the (i) Ca:Si ratio, (ii) the relative proportions Al, Fe, and Mg at fixed ∑MFA, and (iii) the ∑NK added to the deposit on the sulfate decomposition dynamics.

The calculations in set (1) studied the range of temperatures relevant to the experiments. Most of the calculations in sets (2) and (3) were performed at 1025 $^{\circ}$ C, which coincides with significant acceleration of the sulfate decomposition rates in the experiments. In all cases, pure CaSO₄ decomposition was used as a baseline for comparison.

3. Results and discussion

3.1. Experimental determination of sulfate stability and decomposition

Fig. 3 shows the appearance of the $CaSO_4$ and $O\overline{S}$ samples aspressed and after representative heat treatments, and of the oxide samples after the 1225 °C heat treatment. Aside from modest shrinkage, the pellet appearance is unchanged up to 1025 °C. With increasing temperature, the samples darkened, developed a glossy appearance, and then melted. Samples with a glossy appearance while retaining the cylindrical shape are presumed to have a small melt fraction. More significant morphological changes including spreading or dome formation were ascribed to a larger melt fraction or complete melting. Compositions $C_{13}N_{10}K_1M_{11}F_{11}A_{14}S_{40}$ - $O\bar{S}$ and $C_{20}M_5F_5A_{10}S_{60}$ - $O\bar{S}$ showed accelerated shrinkage beginning at 1075 °C and 1125 °C, respectively, indicating their approach to the incipient melting temperature. By 1175 °C the $C_{13}N_{10}K_1M_{11}F_{11}A_{14}S_{40}$ -OS, $C_{15}M_{12}F_{12}A_{16}S_{45}$ -OS, and $C_{20}M_5F_5A_{10}S_{60}$ - $O\bar{S}$ had melted, and $C_{31}M_9F_5A_{12}S_{43}$ - $O\bar{S}$ melted by 1225 °C. The C₁₀M₅F₅A₁₀S₇₀-OS shrank significantly and showed indication of initial melting but retained its pellet shape at 1225 °C. The lower melting onset for $C_{13}N_{10}K_1M_{11}F_{11}A_{14}S_{40}$ -OS is consistent with the presence of the lower-melting Na and K oxides and sulfates. The trends in relative melting temperature are generally consistent with the calculated values in Table 1. However, the high experimental melting point for $C_{31}M_9F_5A_{12}S_{43}$ - $O\bar{S}$ is more consistent with the calculated T_m for the oxide rather than $O\overline{S}$ deposit shown in Table 1. As confirmed in later results, this behavior suggests that the sulfate decomposes fast enough that the $O\overline{S}$ deposit behaves as though it only contains oxides after heating to a high temperature. Similar melting behavior was observed for the oxide samples that,

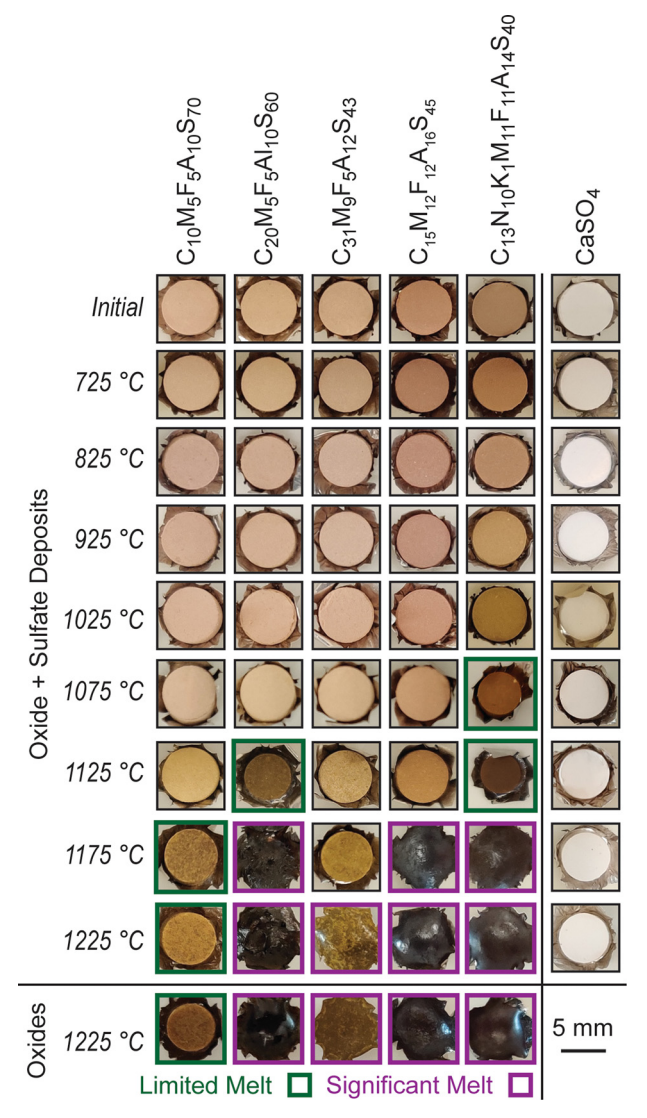


Fig. 3. Photos of mixed oxide + sulfate $(O\overline{S})$, CaSO₄, and mixed oxide samples before and after selected 10 h heat treatments in dry air.

except for $C_{10}M_5F_5A_{10}S_{70}$ -O were significantly molten at 1225 °C. CaSO $_4$ showed no change in physical appearance other than densification

Each heat-treated sample mass was normalized to the starting sample mass after accounting for dehydration at 300 °C. The results are shown in Fig. 4. The $O\bar{S}$ samples begin to lose mass above 725 °C. The retained mass decreases with increasing annealing temperature until reaching the expected mass in the case that the sulfates decompose into the corresponding oxides. Conversely, the oxide samples retain their initial mass to 1225 °C except for a small (~2 %) mass loss for $C_{13}N_{10}K_1M_{11}F_{11}A_{14}S_{40}$ –O. The pure CaSO₄ is stable below 1075 °C, and even after 10 h at 1225 °C its retained mass remains well above the relative mass corresponding to complete sulfate decomposition. Based on the collective results, it is reasonable to assume that the mass loss in the $O\bar{S}$ samples is primarily due to sulfate decomposition and SO_2 volatilization.

The inferred fraction of sulfate decomposed in each experiment (*F*) was then calculated by dividing the normalized mass loss by the theoretical mass loss corresponding to complete sulfate decomposition. The experimental values of the fraction of sulfate decomposed are shown in Fig. 5. Experimental uncertainty from the mass measurements arising from the finite balance precision and modest

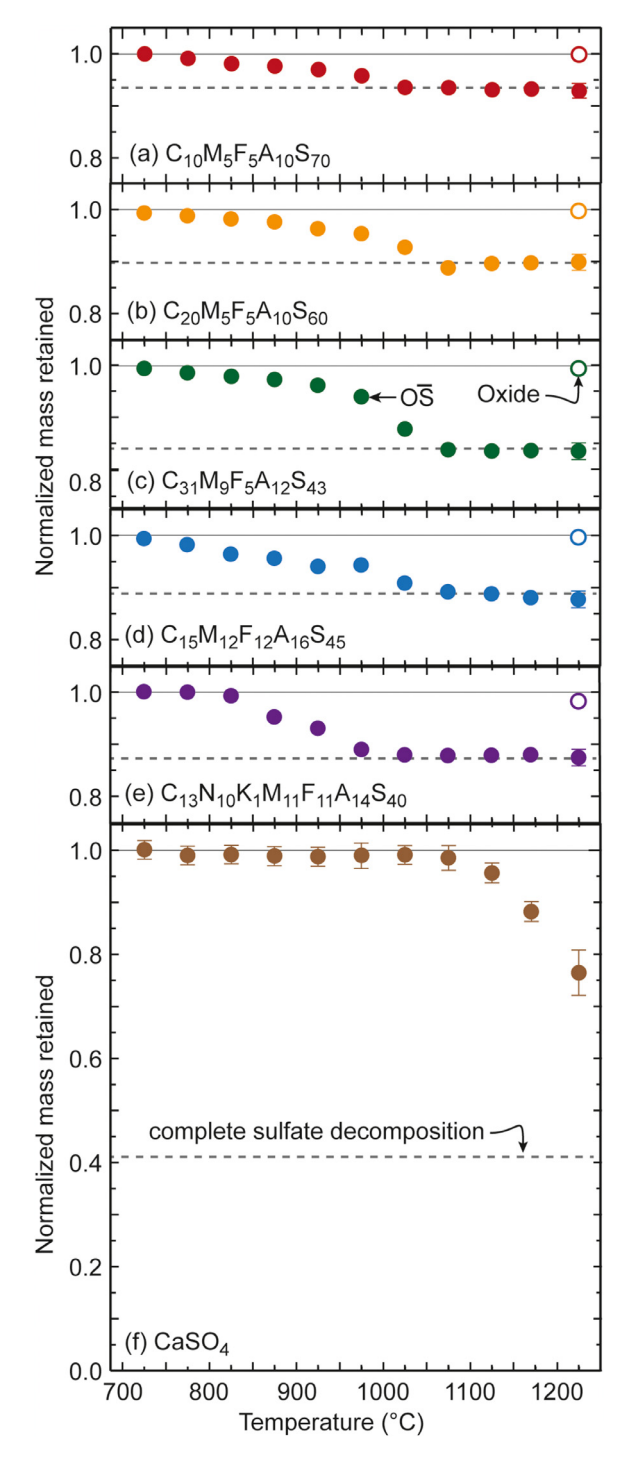


Fig. 4. Normalized mass retained of the $O\overline{S}$ samples (filled circles) and oxide samples (open circles) after 10 h heat treatments in dry air. Some error bars are smaller than the symbols. Most $O\overline{S}$ samples plateau near the mass corresponding to complete sulfate decomposition (indicated by horizontal dashed lines) by 1025 °C.

mass gain due to hydration during sample transfer and weighing was propagated through this calculation to generate the error bars. Small deviations above F=1 at high temperatures in Fig. 5 are likely due to measurement uncertainty or unaccounted moisture in the initial samples. The curve fits in Fig. 5 are based on a generalized logistic function

$$F(T) = \frac{1}{(1 + e^{-A(T-B)})^{C}}$$
 (1)

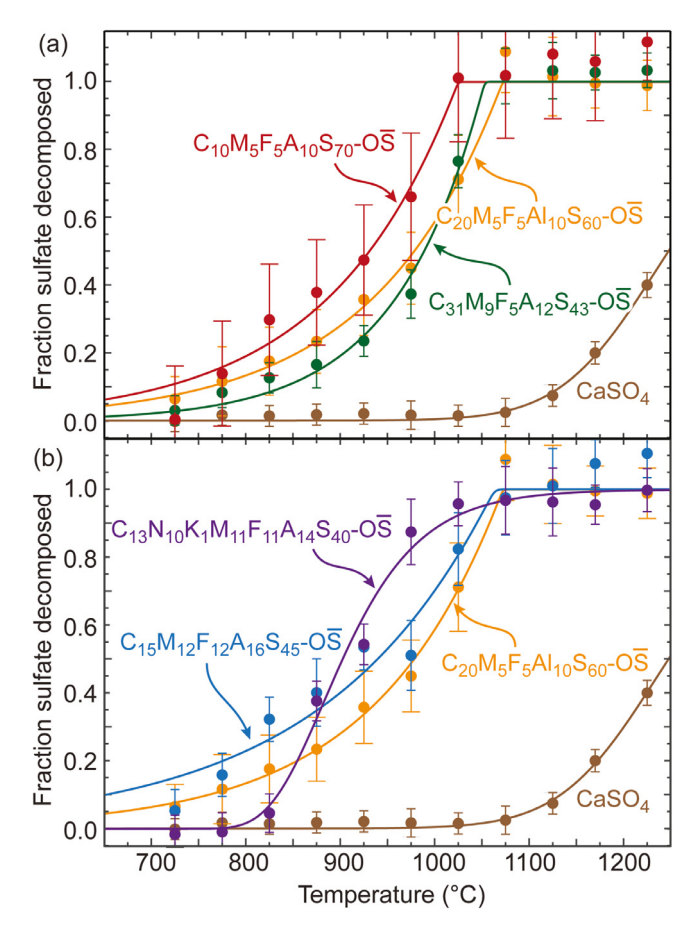


Fig. 5. Assumed fraction of sulfate decomposed after 10 h isothermal anneals in dry air e, calculated assuming that all mass loss above 300 °C is attributed sulfate decomposition. The effects of changing the Ca:Si ratio are illustrated in (a) while the effect of increasing the MFA(NK) content is illustrated in (b). Data for pure CaSO₄ and $C_{20}M_5F_5A_{10}S_{60}$ -OS samples are shown in both panels for comparison.

where the fitting parameters A, B, and C reflect the rate of temperature-dependent accelerated decomposition, the temperature midpoint of the decomposition process, and the skewness toward faster decomposition at higher temperatures, respectively. The key observations include:

- 1. For the $O\overline{S}$ samples, there is modest sulfate decomposition after 10 h at 725 °C and 775 °C. Sulfate decomposition accelerates as the temperature increases, and most of the sulfate is decomposed after 10 h at 1075 °C. Conversely, minimal decomposition of pure CaSO₄ occurs in 10 h below 1075 °C, and the CaSO₄ only partially decomposes in 10 h at higher temperatures.
- 2. Fig. 5(a) compares the results for $C_{10}M_5F_5A_{10}S_{70}$ - $O\bar{S}$, $C_{20}M_5F_5A_{10}S_{60}$ - $O\bar{S}$ and $C_{31}M_9F_5A_{12}S_{43}$ - $O\bar{S}$ to illustrate the effect of changing Ca:Si ratio. The three compositions show similar trend, but the curve for the higher SiO_2 $C_{10}M_5F_5A_{10}S_{70}$ - $O\bar{S}$ composition is shifted to lower temperatures. (Note: the crossover in the fit lines for $C_{20}M_5F_5A_{10}S_{60}$ - $O\bar{S}$ and $C_{31}M_9F_5A_{12}S_{43}$ - $O\bar{S}$ is due only to the change in relative position for the points in the 1025 °C experiment, which is likely doesn't correspond to a different overall trend for the $C_{31}M_9F_5A_{12}S_{43}$ - $O\bar{S}$ composition).
- 3. Fig. 5(b) shows the effects of changing the MFA(NK) content. The $C_{15}M_{12}F_{12}A_{16}S_{45}$ - $O\bar{S}$ composition shows the broadest temperature range for decomposition. The accelerated mass loss at lower temperatures could be associated with the higher fraction of the less-stable MgSO₄ compared to CaSO₄ or as elaborated below, the activation of a reaction pathway producing higher equilibrium p_{SOx} in the initial stages of the reactions.

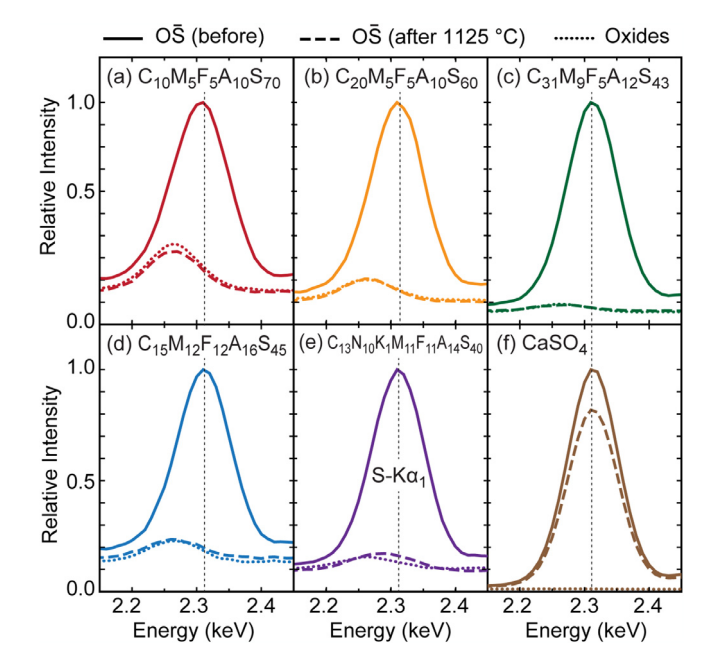


Fig. 6. EDS spectra in the vicinity of sulfur-K α_1 characteristic energy for the assynthesized and 1125°C $O\overline{S}$ sampled and the corresponding oxide sample.

4. Adding sodium and potassium oxides and sulfates $(C_{13}N_{10}K_1M_{11}F_{11}A_{14}S_{40}-O\bar{S}, Fig. 5(b))$ narrows the temperature range for sulfate decomposition. The mass is essentially unchanged until 825 °C, with a rapid increase in sulfate decomposition at higher temperatures. However, the results for this composition reach a plateau slightly below F(T) = 1 at higher temperatures. The implication is that a small fraction (5 to 10%) of the sulfate is retained even at higher temperatures.

EDS was used to confirm that sulfur was removed from the annealed samples. Portions of the spectra in the vicinity of the sulfur- $K\alpha_1$ energy (2.307 keV) are shown in Fig. 6 for the as-synthesized oxide and $O\overline{S}$ samples (Fig. 6(a-e)), and CaSO₄ (Fig. 6(f), with CaO), and the 1125°C heat treated samples. Prior to plotting, the EDS spectra were normalized to the intensity of the primary cation, i.e., Si $K\alpha_1$ for $O\overline{S}$ samples and $Ca K\alpha_1$ for $CaSO_4$ and scaled to produce equivalent initial S $K\alpha_1$ peak intensity. Each of the as-synthesized (before) sulfate-containing samples shows a clear S K α_1 peak. The mixed oxide samples (but not pure CaO) do not have intensity above the Bremsstrahlung at 2.307 keV but do have a low intensity peak near 2.26 keV. This intensity is thought to originate as a secondary signal generated by SiO₂, not by sulfur. The spectra for all the 1125 °C $O\overline{S}$ samples except $C_{13}N_{10}K_1M_{11}F_{11}A_{14}S_{40}$ - $O\overline{S}$ were nearly coincident with the corresponding oxide curves, confirming that the sulfur had been eliminated. A small residual intensity around 2.307 keV for $C_{13}N_{10}K_1M_{11}F_{11}A_{14}S_{40}$ -OS suggests that a small fraction of sulfur remains. For CaSO₄, the S K α_1 peak decreases slightly after heat treatment at 1125 °C but a significant fraction of the sulfur remains. This semi-quantitative EDS data aligns well with the retained mass data, which showed that the 1125 °C $O\overline{S}$ samples except $C_{13}N_{10}K_1M_{11}F_{11}A_{14}S_{40}$ - $O\overline{S}$ should have lost all of their sulfate, the $C_{13}N_{10}K_1M_{11}F_{11}A_{14}S_{40}\text{-}O\bar{S}$ should have a small fraction of retained sulfate, and the CaSO₄ sample should contain \sim 90% of the original sulfate.

3.2. Sulfate decomposition pathway calculations

The first calculations compared individual sub-reactions involved in sulfate decomposition in complex deposits. Fig. 7(a) shows the p_{SO2} for the decomposition of the individual pure sul-

fates. At 1025 °C the relatively high p_{SO2} for MgSO₄ decomposition (0.3 atm) limits the transport-based kinetic hindrance for MgSO₄ decomposition. The p_{SO2} above CaSO₄ is considerably lower (3 \times 10⁻⁶ atm), consistent with the limited decomposition observed at this temperature. The decomposition p_{SO2} for Na₂SO₄ and K₂SO₄ is even lower, suggesting that these sulfates are unlikely to decompose if retained in the condensed deposit at this temperature.

Fig. 7(b) shows the equilibrium p_{SO2} for reactions between specific sulfates and oxides in equimolar ratios. In each case, the p_{SO2} above the decomposing sulfate increases compared to the pure sulfate. The magnitude for the increase when adding oxides to CaSO₄ is significantly greater than when adding oxides (e.g., SiO₂) to $MgSO_4$, given that the latter already has a high equilibrium p_{SO2} . Reacting CaSO₄ with Al₂O₃ or SiO₂ at 1025 °C increases the p_{SO2} by approximately 2.5 or 3.5 orders of magnitude due to the driving force to form CaAl2O4 or CaSiO3, respectively. Adding Fe2O3 with SiO₂ increases p_{SO2} slightly for reactions forming calcium ferro silicates (CFS) like Ca₃Fe₂Si₃O₁₂. Adding MgO along with SiO₂ has a more pronounced effect in increasing the p_{SO2} by forming calcium magnesium silicate (CMS), CaMgSi₂O₆. The p_{SO2} above CaSO₄ at 1025 °C is highest when Al₂O₃ and SiO₂ are both added, stabilizing the calcium aluminum silicate (CAS) anorthite, CaAl₂Si₂O₈. One implication is that the decomposition rate would be maximized for deposits containing sufficient quantities of multiple oxide reactants to convert the sulfate into a mixture of ternary silicates. However, the complete consumption of one reactant could then significantly reduce the p_{SO2} as the decompositions proceed.

Fig. 7(c) shows the initial p_{SO2} above $O\bar{S}$ deposits studied experimentally at 1025 °C. They are significantly higher than pure CaSO₄ (consistent with the faster $O\bar{S}$ decomposition) and cluster near the center of the range for the individual binary and ternary reactions shown in Fig. 7(b). The p_{SO2} for the individual deposits spans approximately an order of magnitude, and the relative positions are generally consistent with the rate of decomposition observed in the experiments.

3.3. Calculated sulfate decomposition pathways for oxide-sulfate deposits

Fig. 8(a) shows the calculated fraction of sulfate decomposed from the five $O\overline{S}$ deposit compositions and pure $CaSO_4$ as a function of the amount air introduced at 1025 °C. These results capture the effect of changes in the reactions as the sulfate decomposition proceeds. The results show that the sulfate in the OS deposits begin to decompose immediately, and that between 10 and 100 moles of air per mole of sulfur must be saturated with SO_x before the sulfate decomposes completely. Conversely, virtually no CaSO₄ decomposition is predicted to occur under the same conditions. This is consistent with the experimental results showing no appreciable mass loss in CaSO₄ at this temperature. In fact, complete decomposition of the CaSO₄ would require saturating at least 2.5×10^5 moles of air per mole of sulfur in the sulfate. A key conclusion is that the reactions between the oxides and sulfates accelerate sulfate decomposition compared to pure CaSO₄.

The rate of sulfate decomposition in the $O\bar{S}$ deposits is approximately linearly proportional to the amount of saturated air (appearing as an exponential increase on the log-linear axis in Fig. 8(a)). Small deviations from the overall trend are due to changes in the reaction pathway as one or more oxide reactants are depleted. Sulfate decomposition is initially fastest in $C_{15}M_{12}F_{12}A_{16}S_{45}$ - $O\bar{S}$, driven by MgSO₄ decomposition and formation of CAS. Beyond $\chi_{air/S}=4$, the curve is coincident with the $C_{10}M_5F_5A_{10}S_{70}$ - $O\bar{S}$ due to formation of CMS in both the deposits. Such behavior is also consistent with the experimental trends.

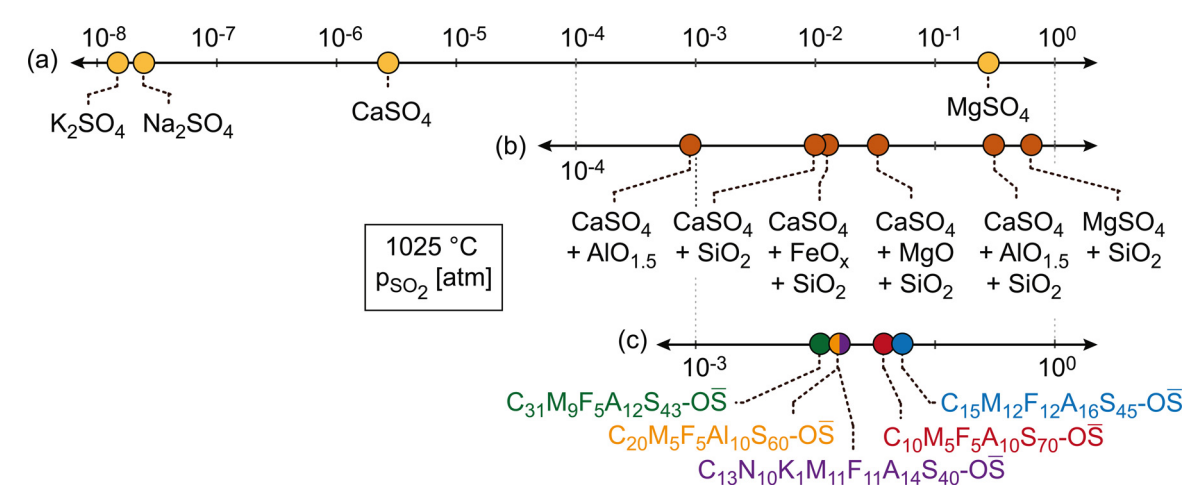


Fig. 7. Equilibrium partial pressure of SO₂ (p_{SO2}) for decomposition of sulfates at 1025 °C in dry air. (a) The wide decomposition p_{SO2} range for the pure sulfates increases for (b) reactions involving other oxides. The p_{SO2} range narrows for (c) the mixed oxide-sulfate deposits studied experimentally.

The curves for $C_{13}N_{10}K_1M_{11}F_{11}A_{14}S_{40}$ – $O\bar{S}$, $C_{20}M_5F_5A_{10}S_{60}$ – $O\bar{S}$, and $C_{31}M_9F_5A_{12}S_{43}$ – $O\bar{S}$ are also clustered due to similar reaction pathways within each group. Until $\chi_{air/S}=10$, all three produce a combination of CAS, ferro silicate (FS), and magnesium silicate (MS) reaction products. CaSiO₃ becomes the dominant reaction product as the Mg, Al, and Fe are consumed, and slight differences in the curves arise due to differences in the $\chi_{air/S}$ required to reach this point. The decomposition rate for $C_{13}N_{10}K_1M_{11}F_{11}A_{14}S_{40}$ drops slightly around $\chi_{air/S}=100$ due to stabilization of the sulfate in the small fraction of liquid generated by the low-melting sodium and potassium compounds.

To capture the temperature dependence of the reactions, calculations were repeated over the experimental temperature range. Fig. 8(b) shows the significant temperature-dependence in the p_{SO2} , while the relative positions of the p_{SO2} for each deposit or mixture at a given temperature is similar to those shown in Fig. 7. To relate the equilibrium calculations to the fixed-time basis of the experiments, the fraction sulfate decomposed was then evaluated for each deposit composition at each temperature for a fixed $\chi_{air/S}$. The flow dynamics in the furnace tube make it difficult to estimate the volume of saturated air in each experiment, especially since multiple parameters related to gaseous flow and diffusion are sensitive to temperature and the position in the reaction boat. Instead, a sensible estimate of $\chi_{air/S} = 100$ was adopted for all temperatures and the results were fitted to generalized logistic function (Eq. (1)) to generate the temperature-dependent, 'fixed-time' decomposition curves shown in Fig. 8(c).

These curves show similarity to the experimental curves shown in Fig. 5. Comparing the cluster of $O\overline{S}$ curves with $CaSO_4$ shows the effect of the oxides in accelerating sulfate decomposition at lower temperatures. Comparing the trend of C₁₀M₅F₅A₁₀S₇₀-OS and C₂₀M₅F₅A₁₀S₆₀-OS, which differ only in Ca:Si ratio, suggests that increasing the Ca:Si ratio slows the sulfate decomposition due to the reduced availability of SiO2 as a reactant. Comparing the decomposition trend of $C_{15}M_{12}F_{12}A_{16}S_{45}$ - $O\bar{S}$ and $C_{20}M_{5}F_{5}A_{10}S_{60}$ - $O\bar{S}$, which differ only in $\sum MFA$, shows how the secondary cations can accelerate sulfate decomposition. The sulfate retained in the liquid in the $C_{13}N_{10}K_1M_{11}F_{11}A_{14}S_{40}$ -OS remains even at higher temperatures, leading that curve to plateau just below F = 1 in Fig. 8(c). Although these calculations capture the relative decomposition order and peak decomposition temperature reasonably well, the experiments showed more decomposition at lower temperature compared to the calculations. This difference could be due to metastable effects (e.g., fast, early decomposition of MgSO₄ in the experiments, compared to the equilibrium decomposition of (Ca,Mg)SO $_4$ in the calculations) or because the $\chi_{air/S}$ value is approximate.

3.4. Composition effects determining sulfate decomposition behavior

Considering the significant effect of deposit composition on the sulfate stability, subsequent calculations systematically explored key composition variables including the Ca:Si ratio, the relative Mg, Fe, and Al ratios, $\sum MFA$ content, and the $\sum NK$ content.

3.4.1. Effect of Ca:Si ratio

Two sets of calculations were performed to assess the role of the Ca:Si ratio on the sulfate decomposition process. The first is based on the $C_{10}M_5F_5A_{10}S_{70}-O\bar{S}$ and $C_{20}M_5F_5A_{10}S_{60}-O\bar{S}$ deposits, which have $\sum MFA=20$. This set was expanded to vary the Ca:Si ratio from no Si to no Ca; i.e. $C_{80}M_5F_5Al_{10}S_0-O\bar{S}$ to $C_0M_5F_5Al_{10}S_{80}-O\bar{S}$. The results showing the fraction of sulfate decomposed as a function of $\chi_{air/S}$ at 1025 °C are shown in Fig. 9(a).

The Ca:Si ratio has a profound effect on the rate of sulfate decomposition. The behavior can be divided into four categories. For a deposit without Ca^{2+} (Ca:Si=0:80), the MgSO₄ decomposes immediately at 1025 °C. This result is consistent with the hierarchy of reactions shown in Fig. 7. Adding Ca^{2+} (as CaO and CaSO₄) increases $\chi_{\text{air/S}}$ required for decomposition of sulfates. For Ca:Si < 1, the sulfates decompose quickly. The curves for Ca:Si = 0.33 (20:60) to 1 (40:40) fall atop one another, suggesting a common reaction pathway. The decomposition rate decreases by orders of magnitude for Ca:Si between 1 and 3, signaling a change in the reaction pathway for the SiO₂-lean deposit compositions. There is a critical minimum SiO₂ content near Ca:Si = 3 (60:20) to drive the accelerated decomposition reactions. For Ca:Si > 3, the sulfate decomposition rate is comparable to pure CaSO₄ even though those mixed deposits still contain Al₂O₃, MgO and Fe₂O₃.

The calculations shown in Fig. 7 indicate that reactions between CaSO₄ and Fe, Mg, and Al oxides also increase the p_{SO2} , and thus should accelerate the decomposition. To understand the effect of these constituents relative to the Ca:Si ratio, the calculations were repeated for deposits with $\sum MFA = 40$, based on $C_{15}M_{12}F_{12}A_{16}S_{45}$ -OS. The results, shown in Fig. 9(b), indicate that in some cases, e.g., Ca:Si = 1:3 and 3:1, the increased $\sum MFA$ accelerates the sulfate decomposition for an equivalent Ca:Si ratio. The accelerated decomposition on increasing $\sum MFA$ arises due to greater formation of CMS, CFS, and CAS, which have higher equilibrium p_{SO2} than the binary compounds. In other cases, e.g., Ca:Si = 1:1, increasing $\sum MFA$ retards the sulfate decomposition initially but then follows

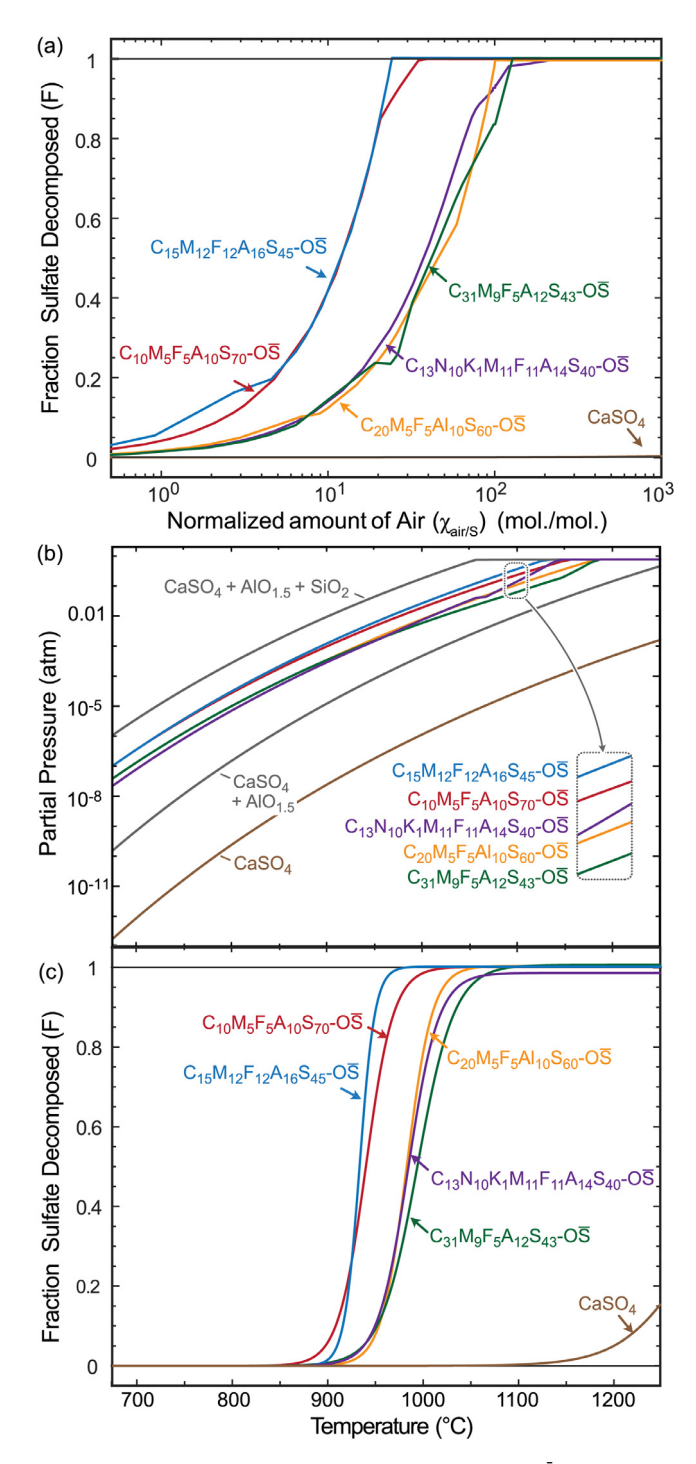


Fig. 8. (a) Equilibrium sulfate decomposition behavior for the $O\overline{S}$ deposits studied experimentally as a function of normalized air supplied at $1025^{\circ}C$. (b) Temperature-dependent equilibrium p_{SO2} above specific mixtures and the $O\overline{S}$ deposits. (c) Equilibrium sulfate decomposition behavior for a set of $O\overline{S}$ deposits as a function of temperature at $\chi_{air/S}=100$ mol./mol in comparison to pure CaSO₄ sulfate decomposition under similar conditions.

similar decomposition rate suggesting similar reaction pathways. The higher \sum MFA has no apparent effect on the sulfate decomposition kinetics for the most SiO₂-lean compositions.

3.4.2. Effect of relative Mg, Al, Fe content

Fig. 10 shows results of calculations investigating the effects of relative magnesium, iron, and aluminum concentration (M:F:A) on the critical $\chi_{air/S}$ corresponding to complete sulfate decomposition

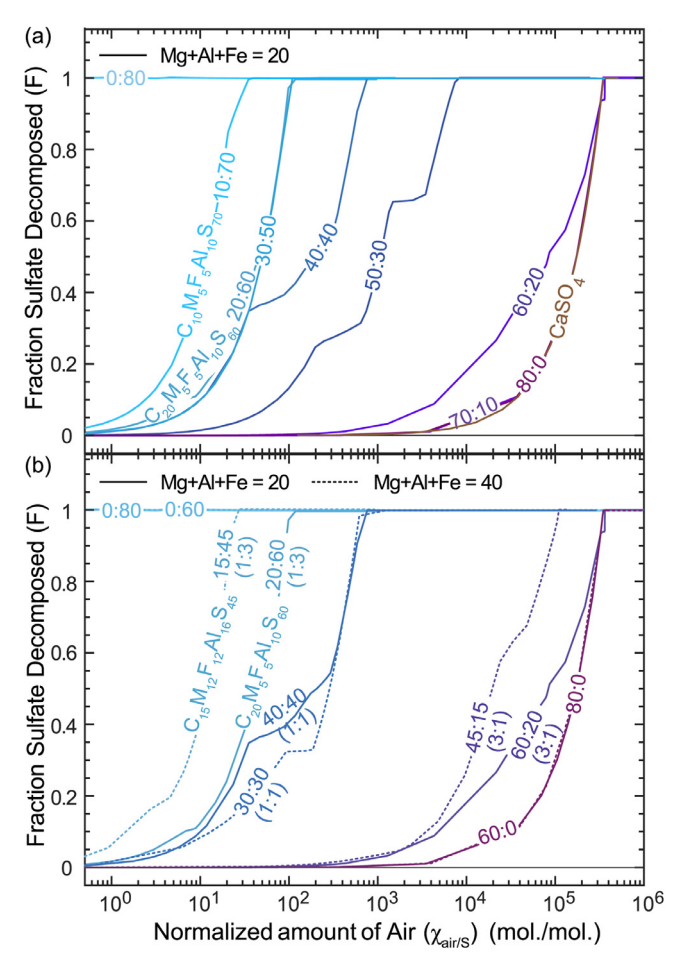


Fig. 9. Equilibrium sulfate decomposition behavior at 1025 °C as a function of $\chi_{\text{air/S}}$: (a) For a set of CMFAS-O $\bar{\text{S}}$ deposits with varying Ca:Si ratio but fixed $\sum MFA = 20 \text{ mol}\%$. (b) For a group of CMFAS-O $\bar{\text{S}}$ deposits comparing $\sum MFA = 20 \text{ mol}\%$ vs. 40 mol% for several fixed Ca:Si ratios.

and the predominant reaction products formed. The calculations were performed at 1025 °C for fixed Ca:Si = 0.33 and for two different \sum MFA concentration. As with the experiments, for these calculations Mg²⁺ is added with an MgO:MgSO₄ mixture in a molar ratio of 2:1. The behavior of deposits with $\sum MFA = 25 \text{ mol}\%$ (Fig. 10(a)) is divided into three regions. Mg-rich deposits exhibit the sulfate decomposition with the smallest quantity of saturated air (i.e., the fastest decomposition in a flowing system) while the Al-rich deposits require the most saturated air for sulfate decomposition (i.e., the slowest in a flowing system). The relative rate of decomposition in Mg- and Fe-rich deposits, which form CFSs and CMSs, respectively, is consistent with the relative equilibrium p_{SO2} values for these reaction products shown in Fig. 7. The slower sulfate decomposition in Al-rich deposits is counterintuitive given the high equilibrium p_{SO2} when CaSO₄, SiO₂ and Al₂O₃ react to form anorthite (CAS) (see Fig. 7). However, the formation of CAS requires an Al:Ca ratio of 2, while Al:Ca for $C_{18,75}M_0F_0A_{25}S_{56,25}$ is only 1.33. Thus, while rapid sulfate decomposition is initially driven by CAS formation, the remaining sulfate decomposes by forming CaSiO3 at a lower equilibrium pSO2 This change in reaction pathway slows the decomposition in Al-rich deposits at low to intermediate $\sum MFA$ content. The change in reaction pathway can also be seen via the change in dominant reaction products as the relative magnesium, iron, and aluminum concentration is varied (Fig. 10(a)).

Increasing the $\sum MFA$ to 40 mol% (Fig. 10(b)) significantly accelerated the sulfate decomposition in the Al-rich deposits, since

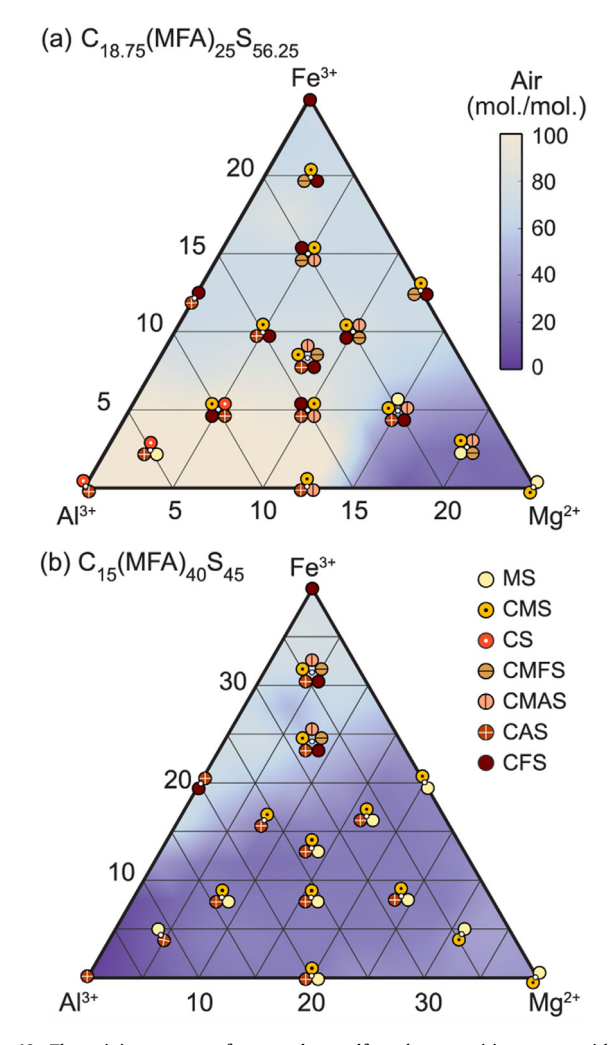


Fig. 10. The minimum $\chi_{air/S}$ for complete sulfate decomposition varys with the relative Mg²⁺, Al³⁺ and Fe³⁺ content for constant Ca:Si ratio for (a) \sum MFA content = 25 mol% (b) \sum MFA content = 40 mol%. The legends specify the primary reaction products calculations at each white point.(MS – MgSiO₃, CMS - calcium magnesium silicates (primarily CaMgSi₂O₆), CS – CaSiO₃, CAS – calcium alumino silicates (primarily CaAl₂Si₂O₈), CFS – calcium ferro silicates (primarily Ca₃Fe₂Si₃O₁₂), CMFS – calcium magnesium ferro silicates, CMAS, calcium magnesium aluminosilicates.

the increased Al:Ca = 2.66 makes anorthite the predominant reaction product until the CaSO₄ is completely decomposed. The decomposition rates for the Mg- and Fe-rich deposits are relatively unchanged compared to \sum MFA = 25 mol%, and the mixed Mg+Ferich deposits show a slight acceleration in sulfate decomposition. This behavior agrees with the distinct reaction pathways observed in CAS, CFS and CMS systems as depicted in Fig. 7. Thus, increasing in the \sum MFA content accelerates the sulfate decomposition by promoting formation of CFSs, CMSs and CASs which form at a much higher p_{SO2} than the products from decomposition of individual sulfates.

3.4.3. Effect of Na+, K+ content

The experiments show that a small fraction of the sulfate in the $C_{13}N_{10}K_1M_{11}F_{11}A_{14}S_{40}$ – $0\bar{S}$ deposit is retained even at high temperatures. The preliminary calculations revealed that at higher temperatures, this sulfate is present in the liquid generated initially by the low melting Na_2SO_4 and K_2SO_4 . This observation supports the hypothesis that a multicomponent ionic liquid could suppress Na_2SO_4 evaporation, thereby increasing the temperature range over which Na_2SO_4 hot corrosion could be active. To further explore the

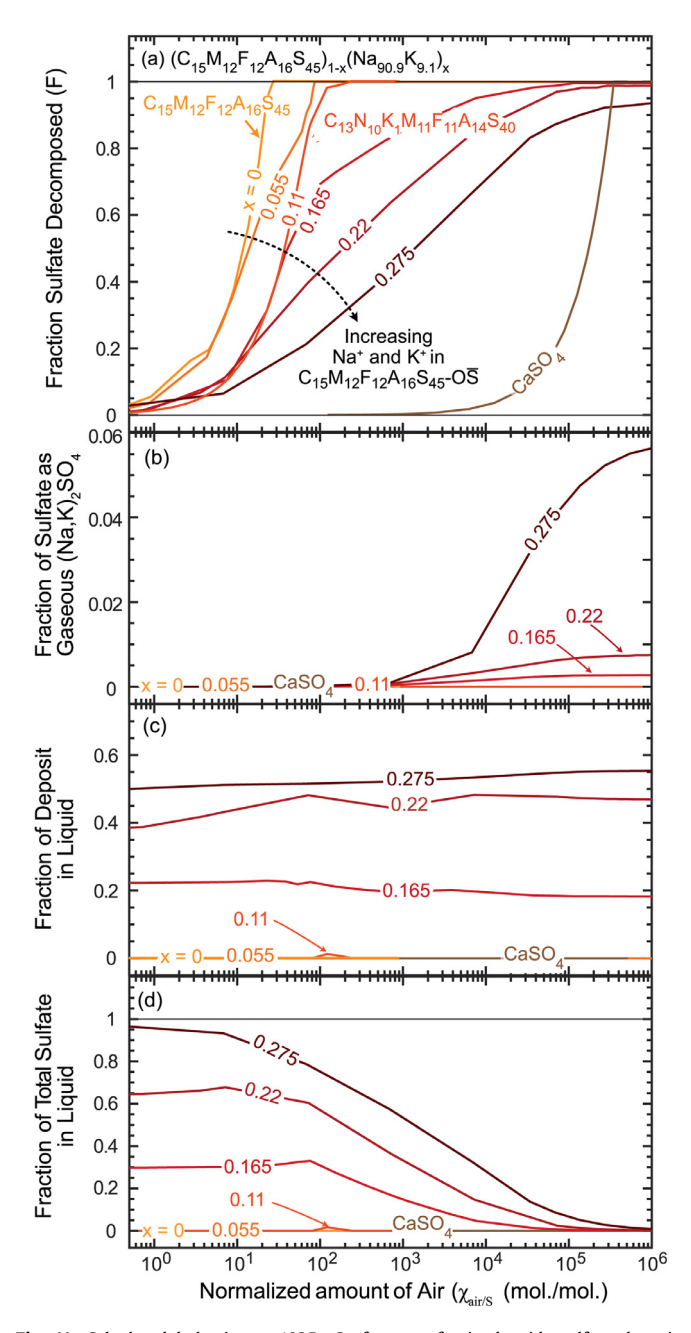


Fig. 11. Calculated behavior at 1025 °C of a set of mixed oxide-sulfate deposits based on $C_{15}M_{12}F_{12}A_{16}S_{45}$ - $0\bar{5}$ with varying Na and K. (a) Equilibrium sulfate decomposition behavior (b) Fraction of initial sulfate present as gaseous Na₂SO₄ and K₂SO₄ (c) Fraction of initial deposit existing as a liquid. (d) Fraction of the initial sulfate present in the melt.

role of sodium and potassium in sulfate stabilization, calculations were performed at 1025 °C for a range of $\sum NK$ up to 25 mol% Na $^+$ according to $(C_{15}M_{12}F_{12}A_{16}S_{45})_{1-x}(N_{90.9}K_{9.1})_x$. In this sequence, x=0.11 corresponds to $C_{13}N_{10}K_1M_{11}F_{11}A_{14}S_{40}$ -05.

The results shown in Fig. 11(a) indicate that increasing $\sum NK$ decreases the rate of sulfate decomposition and increases the $\chi_{air/S}$ required to decompose the sulfates. At x=0.275, the normalized amount of saturated air required to decompose the sulfates at 1025 °C goes beyond that required for pure CaSO₄. Given their relative resistance to decomposition (Fig. 7), Na₂SO₄ and K₂SO₄ evaporation also becomes more important as $\sum NK$ increases. Fig. 11(b) shows that for $x \le 0.11$, the Na₂SO₄ and K₂SO₄ either remain in the condensed deposit or decompose, leaving behind multicompo-

nent oxide reaction products containing Na₂O and K₂O. At higher $\sum NK$ the Na₂SO₄ and K₂SO₄ begin to evaporate, but due to their depressed partial pressures only between one third and one half of these two sulfates enters the gas phase by $\chi_{air/S} = 10^6$ mol/mol.

Fig. 11(c) shows the fraction of the total deposit present as a molten phase. No liquid is formed for x = 0 and x = 0.055. At $x = 0.11 (C_{13}N_{10}K_1M_{11}F_{11}A_{14}S_{40}-O\bar{S})$ a small fraction of liquid is formed at 1025 °C. Further increasing \(\sum NK \) further increases the melt fraction, which remains relatively constant with increasing $\chi_{air/S}$. Fig. 11(d) illustrates how the amount sulfate in the melt relative to the total amount of sulfate initially present varies a function of $\chi_{air/S}$. Once melt begins to form when x = 0.11 $(C_{13}N_{10}K_1M_{11}F_{11}A_{14}S_{40}\text{-}O\bar{S})\!,$ the remaining sulfate dissolves into the melt. With increasing $\sum NK$, the fraction of sulfate in the ionic liquid phase increases significantly. For x = 0.275, virtually all of the sulfate exists initially in the melt. With increasing $\chi_{air/S}$, the fraction of sulfate starts decreasing and the sulfate components in the melt (ionic liquid) decompose to form oxides, along with the limited volatilization of Na₂SO₄ and K₂SO₄ at 1025 °C shown in Fig. 11(b). However, the rate of decomposition is still significantly slower than in the deposits which did not form melt. Thus, presence of significant amount of $\sum NK$ content affects the formation of the ionic liquid, solubility of sulfate entities in the ionic liquid and thus rate of sulfate decomposition.

3.5. Implications for turbine material performance, design, and testing

The results show that the sulfate components of oxide-sulfate mixtures readily decompose in dry air below 1100 °C, even though the decomposition of pure CaSO₄ remains sluggish until higher temperatures. The accelerated sulfate decomposition is driven by reactions between the oxides and sulfates that elevate the equilibrium p_{SO2} above the mixture. Thermodynamic calculations suggest that SiO₂ is the primary driver for these sulfate decomposition pathways. Indeed, the experimental analysis shows that increasing the Ca:Si ratio from $C_{10}M_5F_5A_{10}S_{70}$ - $O\bar{S}$ to $C_{20}M_5F_5A_{10}S_{60}$ - $O\bar{S}$ slows the sulfate decomposition and the calculations suggest that for Ca:Si > 3 the sulfate decomposition would not be significantly accelerated. Mg, Fe, and Al oxides play a secondary role in accelerating the sulfate decomposition when present in sufficient quantity to drive the formation of ternary and quaternary reaction products with greater equilibrium p_{SO2}. Na₂SO₄ and K₂SO₄, which individually volatilize above 950 °C, are stabilized to higher temperatures in multi-cation $O\bar{S}$ deposits through the formation of melts with substantial sulfate solubility. This effect partially underlies the delayed sulfate decomposition in $C_{13}N_{10}K_1M_{11}F_{11}A_{14}S_{40}$ - $O\bar{S}$ compared to $C_{15}M_{12}F_{12}A_{16}S_{45}-O\bar{S}$.

Given that virtually all reported turbine engine deposits fall at Ca:Si < 2 [21], the implication is that most complex deposits forming within an engine would be subject to accelerated sulfate decomposition. Thus, at the temperatures associated with typical CMAS-type attack of TBCs and EBCs, sulfates in a mixed oxidesulfate debris would decompose fast enough that it is likely unnecessary to differentiate between sulfate and non-sulfate deposits when considering ceramic coating degradation at higher temperatures. Indeed, the results show that the $C_{31}M_9F_5A_{12}S_{43}\text{-}0\bar{S}$ composition melts at a temperature closer to that predicted for the oxides, rather than oxide-sulfate mixture, suggesting that the sulfates may decompose before reaching the melting temperature for the oxide-sulfate mixture. Exceptions exist for engines operating in gypsum-rich environments, where Ca:Si is more likely to exceed 3, and in marine environments where higher sodium concentrations are more likely to stabilize sulfates in a multi-component liquid.

The findings also have implications for alloy hot corrosion. First, the stabilization of multicomponent liquid containing sodium sul-

fate to higher temperatures could expand the range of sulfate-induced hot corrosion. The observation that the sulfates in sulfate-oxide mixtures decompose rapidly in the range 900 °C to 1100 °C could reduce the severity of corrosion by removing sulfur from the vicinity of the alloy surface, while the transient spike in p_{SOx} by several orders of magnitude relative to those typically present in the combustion gas could accelerate alloy degradation. These questions remain under study.

Finally, the results highlight the value of thermodynamic calculations as part of an integrated material design and testing framework. The calculations emerge as an essential tool for understanding the reaction pathways governing the sulfate decomposition in the complex deposits. The approach appears to accurately predict both the temperature-dependent nature of the sulfate reactions and the effect of subtle compositional variations on the sulfate decomposition related to pathways involving multi-component reaction products. This approach could be adapted to map the compositional space to identify model deposit compositions expected to efficiently assess a wide range of material behaviors.

4. Conclusions

In this work, experimental and computational tools have been employed to develop a mechanistic understanding of the factors influencing the intrinsic stability of complex, mixed oxide-sulfate deposits. These results are critical to develop an understanding of the accelerated deposit induced degradation of alloys, bond coats and ceramic coatings. Furthermore, this approach can be useful for refining existing thermodynamics models and toolkits that facilitate data driven materials design.

Some key conclusions of this study are as follows:

- 1 Overall composition of the deposit is critical in determining the overall intrinsic stability of the deposit and the rate of sulfate decomposition. The presence of mixed oxides leads to rapid decomposition of the sulfate in the deposit by forming reaction products with high p_{SO2}.
- 2 Deposits with high Ca:Si ratios tend to have slower sulfate decomposition rates with pure CaSO₄ showing the most sluggish decomposition.
- 3 Decomposition of sulfate in deposit compositions with higher Mg, Fe, and Al content is quickened by alternate reaction pathways which form CAS, CMS, and CFS products with high p_{SO2}.
- 4 The presence of Na⁺ and K⁺ ions in the deposits tends to form low melting mixtures with sulfate solubility. This slows down the overall rate of sulfate decomposition.

Declaration of Competing Interest

The authors declare that they have no known competing financial interests or personal relationships that could have appeared to influence the work reported in this paper.

Acknowledgements

This research has been supported by the Office of Naval Research (Award number N68335-20-C-0472 monitored by Dr. David Shifler) in collaboration with QuesTek Innovations LLC. Part of this work was carried out in the Characterization Facility, College of Science and Engineering, University of Minnesota, which receives partial support from the NSF through the MRSEC (Award Number DMR-2011401) and the NNCI (Award Number ECCS-2025124) programs. The sponsors were not involved in the detailed study design, or the data collection, analysis, or interpretation. The authors are grateful to Drs. Pin Lu, Changning Niu, Jiadong Gong (QuesTek Innovations LLC) for insightful discussions.

References

- [1] J. Stringer, Hot corrosion of high-temperature alloys, Annu. Rev. Mater. Sci. 7 (1977) 477–509.
- [2] K.L. Luthra, Low temperature hot corrosion of cobalt-base alloys: part II. Reaction mechanism, Metall. Trans. A 13 (1982) 1853–1864.
- [3] K.L. Luthra, D.A. Shores, Mechanism of Na₂SO₄ induced corrosion at 600 °-900°C, J. Electrochem. Soc. 127 (1980) 2202.
- [4] R.L. Jones, Cobalt oxide-SO₂/SO₃ reactions in cobalt-sodium mixed sulfate formation and low temperature hot corrosion, in: High Temperature Corrosion. Proceedings of the International Conference, San Diego, CA, March 2-6, 1981, p. 1983.
- [5] D.L. Poerschke, R.W. Jackson, C.G. Levi, Silicate deposit degradation of engineered coatings in gas turbines: progress toward models and materials solutions, Annu. Rev. Mater. Res. 47 (2017) 297–330, doi:10.1146/annurev-matsci-010917-105000.
- [6] A.G. Evans, D.R. Clarke, C.G. Levi, The influence of oxides on the performance of advanced gas turbines, J. Eur. Ceram. Soc. 28 (2008) 1405–1419.
- [7] C.G. Levi, J.W. Hutchinson, M.-H. Vidal-Sétif, C.A. Johnson, Environmental degradation of thermal-barrier coatings by molten deposits, MRS Bull. 37 (2012) 932–941.
- [8] F.H. Stott, D.J. De Wet, R. Taylor, Degradation of thermal-barrier coatings at very high temperatures, MRS Bull. 19 (1994) 46–49.
- [9] D.R. Clarke, C.G. Levi, Materials design for the next generation thermal barrier coatings, Annu. Rev. Mater. Res. 33 (2003) 383–417.
- [10] R. Naraparaju, U. Schulz, P. Mechnich, P. Döbber, F. Seidel, Degradation study of 7 wt.% yttria stabilised zirconia (7YSZ) thermal barrier coatings on aero-engine combustion chamber parts due to infiltration by different CaO-MgO-Al₂O₃-SiO₂ variants, Surf. Coat. Technol. 260 (2014) 73–81.
- [11] S. Krämer, S. Faulhaber, M. Chambers, D.R. Clarke, C.G. Levi, J.W. Hutchinson, A.G. Evans, Mechanisms of cracking and delamination within thick thermal barrier systems in aero-engines subject to calcium-magnesium-alumino-silicate (CMAS) penetration, Mater. Sci. Eng. 490 (2008) 26–35.
- [12] K.M. Grant, S. Krämer, J.P. Löfvander, C.G. Levi, CMAS degradation of environmental barrier coatings, Surf. Coat. Technol. 202 (2007) 653–657.
- [13] D.L. Poerschke, J.H. Shaw, N. Verma, F.W. Zok, C.G. Levi, Interaction of yttrium disilicate environmental barrier coatings with calcium-magnesium-iron alumino-silicate melts, Acta Mater. 145 (2018) 451–461.
- [14] F. Stolzenburg, P. Kenesei, J. Almer, K.N. Lee, M.T. Johnson, K.T. Faber, The influence of calcium–magnesium–aluminosilicate deposits on internal stresses in Yb₂Si₂O₇ multilayer environmental barrier coatings, Acta Mater. 105 (2016) 189–198.
- [15] H. Zhao, B.T. Richards, C.G. Levi, H.N. Wadley, Molten silicate reactions with plasma sprayed ytterbium silicate coatings, Surf. Coat. Technol. 288 (2016) 151–162.
- [16] W. Song, Y. Lavallée, K.-U. Hess, U. Kueppers, C. Cimarelli, D.B. Dingwell, Volcanic ash melting under conditions relevant to ash turbine interactions, Nat. Commun. 7 (2016) 1–10.
- [17] D.L. Poerschke, C.G. Levi, Effects of cation substitution and temperature on the interaction between thermal barrier oxides and molten CMAS, J. Eur. Ceram. Soc. 35 (2015) 681–691.
- [18] D.L. Poerschke, T.L. Barth, C.G. Levi, Equilibrium relationships between thermal barrier oxides and silicate melts, Acta Mater. 120 (2016) 302–314.
- [19] E.M. Zaleski, C. Ensslen, C.G. Levi, Melting and crystallization of silicate systems relevant to thermal barrier coating damage, J. Am. Ceram. Soc. 98 (2015) 1642–1649, doi:10.1111/jace.13478.
- [20] P. Mechnich, W. Braue, Volcanic ash-induced decomposition of EB-PVD Gd₂Zr₂O₇ thermal barrier coatings to Gd-oxyapatite, zircon, and Gd, Fezirconolite, J. Am. Ceram. Soc. 96 (2013) 1958–1965, doi:10.1111/jace.12251.
- [21] A.R. Ericks, F.W. Zok, D.L. Poerschke, C.G. Levi, Protocol for selecting exemplary silicate deposit compositions for evaluating thermal and environmental barrier coatings, Under Review (2022).
- [22] V. Tolpygo, Vapor-phase CMAS-induced degradation of adhesion of thermal barrier coatings, Oxid. Met. 88 (2017) 87–96.
- [23] B.S. Lutz, R.W. Jackson, N.M. Abdul-Jabbar, V.K. Tolpygo, C.G. Levi, Water vapor effects on the CMAS degradation of thermal barrier coatings, Oxid. Met. 88 (2017) 73–85.
- [24] D.A. Shifler, S.R. Choi, CMAS effects on ship gas-turbine components/materials, in: ASME Turbo Expo 2018: Turbomachinery Technical Conference and Exposition, American Society of Mechanical Engineers Digital Collection, 2018.
- [25] D.A. Shifler, The Increasing Complexity of Hot Corrosion, American Society of Mechanical Engineers Digital Collection, 2017, doi:10.1115/GT2017-65281.
- [26] D.A. Shifler, Hot corrosion: a modification of reactants causing degradation, Mater. High Temp. 35 (2018) 225–235, doi:10.1080/09603409.2017.1404692.

- [27] T. Gheno, B. Gleeson, Modes of deposit-induced accelerated attack of MCrAlY systems at 1100°C, Oxid. Met. 87 (2017) 249–270.
- [28] T. Gheno, B. Gleeson, On the reaction mechanism of MCrAIY alloys with oxide-sulfate deposits at 1100°C, Oxid Met 86 (2016) 385-406, doi:10.1007/ s11085-016-9649-5.
- [29] M. Kovalchuk, B. Gleeson, Laboratory-scale replication of deposit-induced degradation of high-temperature turbine components, in: S. Tin, M. Hardy, J. Clews, J Cormier, Q. Feng, J. Marcin, C. O'Brien, A. Suzuki (Eds.), Superalloys 2020, Springer International Publishing, Cham, 2020, pp. 789–797, doi:10. 1007/978-3-030-51834-9_77.
- [30] K.Y. Jung, F.S. Pettit, G.H. Meier, The effect of Ca-rich deposits on the high temperature degradation of coated and uncoated superalloys, Mater. Sci. Forum, Trans Tech Publ (2008) 805–812.
- [31] T. Gheno, G.H. Meier, B. Gleeson, High temperature reaction of MCrAlY coating compositions with CaO deposits, Oxid. Met. 84 (2015) 185–209, doi:10.1007/ s11085-015-9550-7.
- [32] M.B. Krisak, B.I. Bentley, A.W. Phelps, T.C. Radsick, Review of calcium sulfate as an alternative cause of hot corrosion, J. Propul. Power 33 (2017) 697–703, doi:10.2514/1.B35936.
- [33] K.J. Meisner, E.J. Opila, Hot corrosion of shipboard gas turbine blades, Oxid. Met. (2020), doi:10.1007/s11085-020-09990-7.
- [34] J.L. Smialek, F.A. Archer, R.G. Garlick, Turbine airfoil degradation in the Persian Gulf war, JOM 46 (1994) 39–41.
- [35] W. Braue, P. Mechnich, Recession of an EB-PVD YSZ coated turbine blade by CaSO₄ and Fe, Ti-rich CMAS-type deposits, J. Am. Ceram. Soc. 94 (2011) 4483–4489.
- [36] P. Mechnich, W. Braue, Solid-state CMAS corrosion of an EB-PVD YSZ coated turbine blade: Zr⁴⁺ partitioning and phase evolution, J. Am. Ceram. Soc. 98 (2015) 296–302.
- 37] P. Patnaik, Handbook of Inorganic Chemicals, McGraw-Hill, New York, 2003.
- [38] D.W. Green, R.H. Perry, Perry's Chemical Engineers' Handbook, McGraw-Hill Education, 2008.
- [39] PubChem, PubChem, (n.d.). https://pubchem.ncbi.nlm.nih.gov/ (accessed January 5, 2022).
- [40] W.M. Swift, A.F. Panek, G.W. Smith, G.J. Vogel, A.A. Jonke, Decomposition of calcium sulfate: a review of the literature (1976).
- [41] E.S. Newman, Behavior of calcium sulfate at high temperatures, J. Res. Nat. Bur. Stand. 27 (1941) 191–196.
- [42] M.N. Scheidema, P. Taskinen, Decomposition thermodynamics of magnesium sulfate, Ind. Eng. Chem. Res. 50 (2011) 9550–9556.
- [43] J.C. Halle, K.H. Stern, Vaporization and decomposition of sodium sulfate. Thermodynamics and kinetics, J. Phys. Chem. 84 (1980) 1699–1704.
- [44] A.D. Gledhill, K.M. Reddy, J.M. Drexler, K. Shinoda, S. Sampath, N.P. Padture, Mitigation of damage from molten fly ash to air-plasma-sprayed thermal barrier coatings, Mater. Sci. Eng. 528 (2011) 7214–7221.
- [45] E. Godbole, A. von der Handt, D. Poerschke, Apatite and garnet stability in the Al-Ca-Mg-Si-(Gd/Y/Yb)-O systems and implications for T/EBC: CMAS reactions, J. Am. Ceram. Soc. 105 (2022) 1596–1609.
- [46] M.P. Borom, C.A. Johnson, L.A. Peluso, Role of environment deposits and operating surface temperature in spallation of air plasma sprayed thermal barrier coatings, Surf. Coat. Technol. 86 (1996) 116–126.
- [47] W.D. Summers, D.L. Poerschke, D. Park, J.H. Shaw, F.W. Zok, C.G. Levi, Roles of composition and temperature in silicate deposit-induced recession of yttrium disilicate, Acta Mater. 160 (2018) 34-46, doi:10.1016/j.actamat.2018. 08.043.
- [48] seawater | Density, Composition, Salinity, Distribution, & Facts | Britannica, January 25, 2022 n.d. https://www.britannica.com/science/seawater (accessed.
- [49] P. Webb, Introduction to oceanography, Roger Williams University, 2021.
- [50] N. Kanari, N.-E. Menad, E. Ostrosi, S. Shallari, F. Diot, E. Allain, J. Yvon, Thermal behavior of hydrated iron sulfate in various atmospheres, Metals 8 (2018) 1084
- [51] P.G. Coombs, Z.A. Munir, The decomposition of iron (III) sulfate in air, J. Therm. Anal. 35 (1989) 967–976.
- [52] C.W. Bale, E. Bélisle, P. Chartrand, S.A. Decterov, G. Eriksson, K. Hack, I.-H. Jung, Y.-B. Kang, J. Melançon, A.D. Pelton, C. Robelin, S. Petersen, FactSage thermochemical software and databases recent developments, Calphad 33 (2009) 295–311, doi:10.1016/j.calphad.2008.09.009.
- [53] C.W. Bale, E. Bélisle, P. Chartrand, S.A. Decterov, G. Eriksson, A.E. Gheribi, K. Hack, I.-H. Jung, Y.-B. Kang, J. Melançon, A.D. Pelton, S. Petersen, C. Robelin, J. Sangster, P. Spencer, M.-A. Van Ende, Reprint of: FactSage thermochemical software and databases, 2010–2016, Calphad 55 (2016) 1–19, doi:10.1016/j.calphad.2016.07.004.
- [54] D.L. Poerschke, Developments in thermodynamic models of deposit-induced corrosion of high-temperature coatings, JOM (2021) 1–14.